

On the Development of a Dynamic Non-linear Closure for Large-Eddy Simulation of the Atmospheric Boundary Layer

Hao Lu · Fernando Porté-Agel

Received: 9 July 2013 / Accepted: 31 December 2013 / Published online: 21 January 2014
© Springer Science+Business Media Dordrecht 2014

Abstract A dynamic procedure is developed to compute the model coefficients in the recently introduced modulated gradient models for both momentum and scalar fluxes. The magnitudes of the subgrid-scale (SGS) stress and the SGS flux are estimated using the local equilibrium hypothesis, and their structures (relative magnitude of each of the components) are given by the normalized gradient terms, which are derived from the Taylor expansion of the exact SGS stress/flux. Previously, the two model coefficients have been specified on the basis of theoretical arguments. Here, we develop a dynamic SGS procedure, wherein the model coefficients are computed dynamically according to the statistics of the resolved turbulence, rather than provided a priori or ad hoc. Results show that the two dynamically calculated coefficients have median values that are approximately constant throughout the turbulent atmospheric boundary layer (ABL), and their fluctuations follow a near log-normal distribution. These findings are consistent with the fact that, unlike eddy-viscosity/diffusivity models, modulated gradient models have been found to yield satisfactory results even with constant model coefficients. Results from large-eddy simulations of a neutral ABL and a stable ABL using the new closure show good agreement with reference results, including well-established theoretical predictions. For instance, the closure delivers the expected surface-layer similarity profiles and power-law scaling of the power spectra of velocity and scalar fluctuations. Further, the Lagrangian version of the model is tested in the neutral ABL case, and gives satisfactory results.

Keywords Atmospheric boundary layer · Large-eddy simulation · Subgrid-scale modelling

1 Introduction

The high Reynolds-number turbulent atmospheric boundary layer (ABL) bears a wide range of turbulent length scales, from millimetres to kilometres. It is difficult to develop a gen-

H. Lu · F. Porté-Agel (✉)
Wind Engineering and Renewable Energy Laboratory (WIRE), École Polytechnique
Fédérale de Lausanne (EPFL), Lausanne, Switzerland
e-mail: fernando.porte-agel@epfl.ch

eral and yet simple turbulence model for climate and mesoscale applications owing to the complex physical processes involved in ABL flows. Since the pioneering work of [Deardorff \(1970, 1972\)](#), large-eddy simulation (LES) has been employed as the most accurate approach to simulate ABL turbulence. The physical basis for LES is the separation of the flow into grid resolved and subgrid-scale (SGS) motions. This is achieved through the use of a three-dimensional spatial filtering operation, denoted here as a tilde (\sim). The resolved motions contain most of the energy, and one can compute them numerically by solving the LES governing equations, while the effects of the less energetic SGS motions are parameterized. Filtering the equations describing the conservation of momentum and scalar concentration (e.g., temperature) results in two extra terms: the SGS stress, τ_{ij} , and the SGS flux, q_i

$$\tau_{ij} = \widetilde{u_i u_j} - \widetilde{u}_i \widetilde{u}_j, \quad (1)$$

and

$$q_i = \widetilde{u_i \theta} - \widetilde{u}_i \widetilde{\theta}, \quad (2)$$

where τ_{ij} and q_i must be closed in terms of the resolved velocity field \widetilde{u}_i and the resolved scalar field $\widetilde{\theta}$.

Small-scale processes in ABL flows, which influence the vertical and horizontal exchange of quantities between the surface and the atmosphere as well as the mixing within the atmosphere, show great sensitivity to the model formulation ([Holtslag 2006](#)). The representation of these processes using an SGS closure is non-trivial owing to the fact that there exist many non-linear processes. Numerous SGS closures have been proposed since the introduction of the first SGS stress model of [Smagorinsky \(1963\)](#). The Smagorinsky model, as the most commonly used model, belongs to the family of eddy-viscosity and eddy-diffusivity models. They are all based on two important assumptions: (i) the effects of the SGS motions on the resolved motions are essentially energetic actions, so that the modelling focuses primarily on the balance of the energy transfers between the two scale ranges, and (ii) the energy-transfer mechanism is analogous to the molecular mechanism represented by diffusion. The local equilibrium hypothesis is often adopted to determine the model coefficients. In the context of ABL flows, the early eddy-viscosity/diffusivity models have revealed that the mean modelled wind and temperature profiles in the surface layer differ from those in experiments and observations following, for example, the Monin–Obukhov similarity forms (e.g., [Businger et al. 1971](#); [Stull 1988](#)). Specifically, the non-dimensional vertical gradients of velocity and temperature could be overestimated by more than 20% in the surface layer. To try and resolve this issue, researchers have introduced quite a few modifications. For instance, [Mason \(1989\)](#) and [Mason and Thomson \(1992\)](#) used an ad hoc expression to provide appropriate SGS mixing lengths; [Sullivan et al. \(1994\)](#) proposed a two-part eddy-viscosity/diffusivity model that includes contributions from the mean flow and the turbulent fluctuations near the surface; [Kosović \(1997\)](#) proposed a non-linear modification that allows for a backward energy cascade; and [Porté-Agel et al. \(2000\)](#) and [Porté-Agel \(2004\)](#) used a scale-dependent dynamic approach to compute the model coefficients dynamically, while allowing for scale dependence of the coefficients.

A major drawback of eddy-viscosity/diffusivity models, found in a priori analyses of fields obtained from experiments and simulations ([Liu et al. 1994](#); [Menon et al. 1996](#); [Porté-Agel et al. 2001](#); [Higgins et al. 2003](#); [Lu et al. 2007](#)), is the low correlation between the exact SGS term and the eddy-viscosity/diffusivity term. [Khanna and Brasseur \(1998\)](#), [Juneja](#)

and Brasseur (1999), and Porté-Agel et al. (2000) have also shown that, on coarse grids, eddy-viscosity models may induce large errors because they are not able to account for the strong flow anisotropy in the ABL surface layer. Further, eddy-viscosity models do not have the same rotation transformation properties as the actual SGS stress tensor, which is not material frame indifferent (MFI). Recent studies (Kobayashi and Shimomura 2001; Horiuti 2006; Lu et al. 2007, 2008) have revisited the importance of the MFI consistency of the modelling SGS stresses. In LES of mesoscale and large-scale atmospheric turbulence including planetary rotation, eddy-viscosity models induce extra errors and yield unsatisfactory results, such as the incapability of capturing cyclone-anticyclone asymmetry (Lu et al. 2008). In addition, eddy-viscosity/diffusivity models are by construction fully dissipative, and do not allow energy transfers from unresolved to resolved scales. However, such inverse energy transfers are known to occur (Cambon et al. 1997; Smith and Waleffe 1999).

The variety of SGS models arises not only because the theoretical justifications are arguable but also because LES solutions are sensitive to the given type of SGS models, especially in the surface layer of ABL flows. In contrast to eddy-viscosity/diffusivity models, gradient models are derived from the Taylor series expansions of the SGS terms that appear in the filtered conservation equations (Clark et al. 1979), do not locally assume the same eddy viscosity/diffusivity for all directions, and make no use of prior knowledge of the interactions between resolved motions and SGS motions. At the a priori level, gradient models generally predict the structure of the exact SGS terms much more accurately than eddy-viscosity/diffusivity models (and therefore are better able to capture anisotropic effects and disequilibrium, e.g., Liu et al. 1994; Porté-Agel et al. 2001; Higgins et al. 2003; Lu et al. 2007, 2008; Chamecki 2010). These features make gradient models attractive. However, when implemented in simulations, traditional gradient schemes are not able to yield the correct levels of SGS production (energy transfer between resolved and SGS scales), and as a result, simulations often become numerically unstable as reported in a variety of contexts (e.g., Sagaut 2006).

A new SGS closure derived from gradient models has been recently introduced (Lu and Porté-Agel 2010, 2013; Lu 2011). Simulation results obtained with the use of this new closure show good agreement with well-established predictions and an evident improvement over results obtained using traditional eddy-viscosity/diffusivity models. On the basis of theoretical arguments, which are strictly valid only in the inertial subrange of high Reynolds-number turbulence, the closure adopts constant values for the two model coefficients. It is, however, arguable that one can effectively model a variety of phenomena present in turbulent flows using two universal constants. A complementary and perhaps more reasonable approach is the dynamic procedure (Germano et al. 1991; Lilly 1992), which is becoming more prevalent in simulations for determining coefficients. Basically, the approach adopts the assumption of scale invariance by applying the coefficients optimised from the resolved scales to the SGS range, accomplished by applying a test filter at a scale slightly larger than the resolved scale ($\hat{\Delta}$). Thus, the model coefficients can be determined on the basis of the resolved flow field without a priori or ad hoc specifications.

In this paper, we present the development of a dynamic non-linear SGS closure in Sect. 2. We test the performance of the new closure in high Reynolds-number simulations of a neutrally stratified ABL case and a stably stratified ABL case. Section 3 describes the governing equations and common numerical set-up, while Sects. 4 and 6 present the LES results. Section 8 summarizes the main results.

2 Dynamic SGS Closure Coupling with a Passive Scalar

The non-linear model formulations introduced by Lu and Porté-Agel (2010, 2013) for the SGS stress tensor, $\tau_{ij} = \widetilde{u_i u_j} - \widetilde{u_i} \widetilde{u_j}$, and for the SGS flux vector, $q_i = \widetilde{u_i \theta} - \widetilde{u_i} \widetilde{\theta}$, can be written as

$$\tau_{ij} = 2k_{sgs} \left(\frac{\widetilde{G}_{ij}}{\widetilde{G}_{kk}} \right), \tag{3}$$

and

$$q_i = |\mathbf{q}| \left(\frac{\widetilde{G}_{\theta,i}}{|\widetilde{\mathbf{G}}_{\theta}|} \right). \tag{4}$$

The method separates the modelling into two elements: the normalized gradient terms serve to model the structure (relative magnitude of each component); and a separate approach is needed for the SGS kinetic energy, $k_{sgs} = \frac{1}{2} \tau_{ii}$, and the magnitude of the SGS flux vector, $|\mathbf{q}|$. To account for the grid anisotropy in the study ($\widetilde{\Delta}_x, \widetilde{\Delta}_y$ and $\widetilde{\Delta}_z$ are not equal), we define $\widetilde{G}_{ij} = \frac{\widetilde{\Delta}_x^2}{12} \frac{\partial \widetilde{u}_i}{\partial x} \frac{\partial \widetilde{u}_j}{\partial x} + \frac{\widetilde{\Delta}_y^2}{12} \frac{\partial \widetilde{u}_i}{\partial y} \frac{\partial \widetilde{u}_j}{\partial y} + \frac{\widetilde{\Delta}_z^2}{12} \frac{\partial \widetilde{u}_i}{\partial z} \frac{\partial \widetilde{u}_j}{\partial z}$, and $\widetilde{G}_{\theta,i} = \frac{\widetilde{\Delta}_x^2}{12} \frac{\partial \widetilde{u}_i}{\partial x} \frac{\partial \widetilde{\theta}}{\partial x} + \frac{\widetilde{\Delta}_y^2}{12} \frac{\partial \widetilde{u}_i}{\partial y} \frac{\partial \widetilde{\theta}}{\partial y} + \frac{\widetilde{\Delta}_z^2}{12} \frac{\partial \widetilde{u}_i}{\partial z} \frac{\partial \widetilde{\theta}}{\partial z}$, and compute the gradient vector's magnitude with the Euclidean norm $|\widetilde{\mathbf{G}}_{\theta}| = \sqrt{\widetilde{G}_{\theta,1}^2 + \widetilde{G}_{\theta,2}^2 + \widetilde{G}_{\theta,3}^2}$. To close the approach, one needs to evaluate the magnitudes k_{sgs} and $|\mathbf{q}|$. Even though a previous approach (Chumakov and Rutland 2005) places much emphasis on the scalar field, it is desirable, owing to the definition of the SGS flux vector as shown in Eq. 2, that the SGS flux magnitude encompasses both the velocity and the scalar fields. Therefore the flux magnitude is modelled as the multiplication of an SGS velocity scale and an SGS scalar concentration scale $|\mathbf{q}| = u_{sgs} \theta_{sgs}$ (Lu and Porté-Agel 2013). It is straightforward to assume that the SGS velocity scale is proportional to the square root of the SGS kinetic energy, $u_{sgs} = C \sqrt{k_{sgs}}$. Further, one can identify the value of k_{sgs} by using the resolved velocities on the basis of the local equilibrium hypothesis, which assumes a balance between the SGS kinetic energy production P ($P = -\tau_{ij} \frac{\partial \widetilde{u}_i}{\partial x_j} = -\tau_{ij} \widetilde{S}_{ij}$, where $\widetilde{S}_{ij} = \frac{1}{2} \left(\frac{\partial \widetilde{u}_i}{\partial x_j} + \frac{\partial \widetilde{u}_j}{\partial x_i} \right)$ is the resolved strain rate tensor) and dissipation rate ε . A classical evaluation of kinetic energy dissipation is $\varepsilon = C_{\varepsilon} \frac{k_{sgs}^{3/2}}{\Delta}$. Simulations allow for no negative dissipation rate, the so-called clipping, leading to

$$k_{sgs} = \mathbf{H}(P) \frac{4\widetilde{\Delta}^2}{C_{\varepsilon}^2} \left(-\frac{\widetilde{G}_{ij}}{\widetilde{G}_{kk}} \widetilde{S}_{ij} \right)^2, \tag{5}$$

where $\mathbf{H}(x)$ is the Heaviside step function defined as $\mathbf{H}(x) = 0$ if $x < 0$ and $\mathbf{H}(x) = 1$ if $x \geq 0$. To predict the SGS scalar concentration scale, again we adopt the local equilibrium hypothesis, which assumes a balance between the SGS scalar variance production, $P_{\theta} = -q_i \frac{\partial \widetilde{\theta}}{\partial x_i}$, and the SGS scalar variance dissipation rate ε_{θ} . A classical evaluation of the SGS scalar variance dissipation rate is $\varepsilon_{\theta} = C_{\varepsilon \theta} \frac{\theta_{sgs}^2 u_{sgs}}{\Delta}$. Using the proposed model formulation, together with the local equilibrium hypothesis, one obtains $\theta_{sgs} = \frac{\widetilde{\Delta}}{C_{\varepsilon \theta}} \left(-\frac{\widetilde{G}_{\theta,i}}{|\widetilde{\mathbf{G}}_{\theta}|} \frac{\partial \widetilde{\theta}}{\partial x_i} \right)$. The SGS scalar variance dissipation rate is always non-negative, thus

$$\theta_{sgs} = \mathbf{H}(P_{\theta}) \frac{\widetilde{\Delta}}{C_{\varepsilon \theta}} \left(-\frac{\widetilde{G}_{\theta,i}}{|\widetilde{\mathbf{G}}_{\theta}|} \frac{\partial \widetilde{\theta}}{\partial x_i} \right). \tag{6}$$

Finally, one obtains the following equation for the magnitude of the SGS flux

$$|\mathbf{q}| = \mathbf{H}(P_\theta) \mathbf{H}(P) \frac{2\sqrt{2}\tilde{\Delta}^2}{C_\varepsilon C_{\varepsilon\theta}} \left(-\frac{\tilde{G}_{\theta,i}}{|\tilde{\mathbf{G}}_\theta|} \frac{\partial \tilde{\theta}}{\partial x_i} \right) \left(-\frac{\tilde{G}_{ij}}{\tilde{G}_{kk}} \tilde{S}_{ij} \right), \tag{7}$$

where $C = \sqrt{2} (u_{\text{sgs}} = \sqrt{(\widetilde{u_i u_i} - \tilde{u}_i \tilde{u}_i)} = \sqrt{2 k_{\text{sgs}}})$ has been assumed. Constant coefficients (C_ε and $C_{\varepsilon\theta}$) were used in previous simulations (Lu and Porté-Agel 2010, 2013; Lu 2011). Even though results turned out to be reasonably satisfactory, it should be noted that the selected constant values rest on theoretical arguments that are strictly valid only in the inertial subrange of high Reynolds-number turbulence. Further, for complex flows, it may not be possible to find universal constants that are appropriate for the entire domain at all times.

A more systematic way to compute the SGS model coefficients is to use the so-called dynamic procedure, which is based on the Germano identities (Germano et al. 1991; Lilly 1992) for the SGS stress tensor and the SGS flux vector,

$$L_{ij} = T_{ij} - \bar{\tau}_{ij} = \overline{\tilde{u}_i \tilde{u}_j} - \tilde{u}_i \tilde{u}_j, \tag{8}$$

and

$$K_i = Q_i - \bar{q}_i = \overline{\tilde{u}_i \tilde{\theta}} - \tilde{u}_i \tilde{\theta}, \tag{9}$$

where $T_{ij} = \overline{\tilde{u}_i \tilde{u}_j} - \tilde{u}_i \tilde{u}_j$ and $Q_i = \overline{\tilde{u}_i \tilde{\theta}} - \tilde{u}_i \tilde{\theta}$ are the stress and the flux at a test-filter scale $\bar{\Delta} = \alpha \tilde{\Delta}$ (typically $\alpha = 2$). L_{ij} and K_i can be evaluated on the basis of the resolved scales. Applying the dynamic procedure to the modulated gradient model, T_{ij} and Q_i are determined by

$$T_{ij} = \frac{8}{C_\varepsilon^2} \alpha^2 \tilde{\Delta}^2 \left(-\frac{\overline{\tilde{G}_{mn}}}{\overline{\tilde{G}_{kk}}} \overline{\tilde{S}_{mn}} \right)^2 \left(\frac{\overline{\tilde{G}_{ij}}}{\overline{\tilde{G}_{ll}}} \right), \tag{10}$$

$$Q_i = \frac{2\sqrt{2}\alpha^2 \tilde{\Delta}^2}{C_{\varepsilon\theta} C_\varepsilon} \left(-\frac{\overline{\tilde{G}_{\theta,j}}}{|\overline{\tilde{\mathbf{G}}_\theta}|} \frac{\partial \overline{\tilde{\theta}}}{\partial x_j} \right) \left(-\frac{\overline{\tilde{G}_{mn}}}{\overline{\tilde{G}_{kk}}} \overline{\tilde{S}_{mn}} \right) \left(-\frac{\overline{\tilde{G}_{\theta,i}}}{|\overline{\tilde{\mathbf{G}}_\theta}|} \right). \tag{11}$$

In order not to confuse the clipping procedure with the dynamic procedure and numerically leave more clippings in the flow, we do not consider clipping here. Hence, the Germano identities (Eqs. 8 and 9) can be re-written as

$$T_{ij} - \bar{\tau}_{ij} = \frac{1}{C_\varepsilon^2} M_{ij}, \tag{12}$$

and

$$Q_i - \bar{q}_i = \frac{1}{C_{\varepsilon\theta} C_\varepsilon} X_i, \tag{13}$$

where

$$M_{ij} = 8\alpha^2 \tilde{\Delta}^2 \left(-\frac{\overline{\tilde{G}_{mn}}}{\overline{\tilde{G}_{kk}}} \overline{\tilde{S}_{mn}} \right)^2 \left(\frac{\overline{\tilde{G}_{ij}}}{\overline{\tilde{G}_{ll}}} \right) - 8\tilde{\Delta}^2 \left(-\frac{\overline{\tilde{G}_{mn}}}{\overline{\tilde{G}_{kk}}} \overline{\tilde{S}_{mn}} \right)^2 \left(\frac{\overline{\tilde{G}_{ij}}}{\overline{\tilde{G}_{ll}}} \right), \tag{14}$$

and

$$\begin{aligned}
 X_i &= 2\sqrt{2}\alpha^2\tilde{\Delta}^2 \left(-\frac{\tilde{G}_{\theta,j}}{|\tilde{G}_{\theta}|} \frac{\partial\tilde{\theta}}{\partial x_j} \right) \left(-\frac{\tilde{G}_{mn}}{\tilde{G}_{kk}} \tilde{S}_{mn} \right) \left(-\frac{\tilde{G}_{\theta,i}}{|\tilde{G}_{\theta}|} \right) \\
 &\quad - 2\sqrt{2}\tilde{\Delta}^2 \left(-\frac{\tilde{G}_{\theta,j}}{|\tilde{G}_{\theta}|} \frac{\partial\tilde{\theta}}{\partial x_j} \right) \left(-\frac{\tilde{G}_{mn}}{\tilde{G}_{kk}} \tilde{S}_{mn} \right) \left(-\frac{\tilde{G}_{\theta,i}}{|\tilde{G}_{\theta}|} \right). \tag{15}
 \end{aligned}$$

Minimising the error associated with the use of the model formulation (Eqs. 3 and 4) in the Germano identity (Eqs. 8 and 9) over all independent components (Lilly 1992), one obtains the evaluation expressions for C_ε and $C_{\varepsilon\theta}$

$$(C_\varepsilon)^{-2} = \frac{L_{ij}M_{ij}}{M_{ij}M_{ij}}, \tag{16}$$

and

$$(C_{\varepsilon\theta}C_\varepsilon)^{-1} = \frac{K_iX_i}{X_jX_j}. \tag{17}$$

In practice, the above equations do not guarantee positive values for $(C_\varepsilon)^{-2}$ and $(C_{\varepsilon\theta}C_\varepsilon)^{-1}$, where positive values are necessary to ensure numerical stability. When negative coefficient values are encountered, following Lu and Porté-Agel (2010, 2013), we assign $C_\varepsilon = 1$ and $C_{\varepsilon\theta} = 1$.

3 Numerical Simulations

Previous studies (e.g., Andren et al. 1994; Sullivan et al. 1994) have stated that the discrepancy between simulation results and surface-layer similarity theory becomes more evident as surface buoyancy forcing decreases. In this regard, one should expect a larger impact of the SGS formulation in neutral and stable cases than in convective (unstable) cases. Here, we focus on two cases: one involves neutral stability conditions, and the other involves stably stratified conditions. Also, because the simulated flows have high Reynolds numbers (commonly $O(10^8)$ or larger), no near-wall viscous processes are resolved, and the viscous terms are neglected in the governing equations.

We use a modified LES code that has been used for previous studies (e.g., Albertson and Parlange 1999; Porté-Agel et al. 2000; Porté-Agel 2004; Stoll and Porté-Agel 2006a,b, 2008; Lu and Porté-Agel 2010). The code solves the filtered equations of continuity, conservation of momentum and scalar transport

$$\frac{\partial\tilde{u}_i}{\partial x_i} = 0, \tag{18}$$

$$\frac{\partial\tilde{u}_i}{\partial t} + \frac{\partial\tilde{u}_i\tilde{u}_j}{\partial x_j} = -\frac{\partial\tilde{p}}{\partial x_i} - \frac{\partial\tau_{ij}}{\partial x_j} + \tilde{f}_i, \tag{19}$$

$$\frac{\partial\tilde{\theta}}{\partial t} + \tilde{u}_i \frac{\partial\tilde{\theta}}{\partial x_i} = -\frac{\partial q_i}{\partial x_i}, \tag{20}$$

where $(\tilde{u}_1, \tilde{u}_2, \tilde{u}_3) = (\tilde{u}, \tilde{v}, \tilde{w})$ are the components of the resolved velocity field, $\tilde{\theta}$ is the resolved scalar, \tilde{p} is the effective pressure, and \tilde{f}_i is a forcing term. In the stable case, the buoyancy force and the Coriolis force would be included as $\tilde{f}_i = \delta_{i3}g\frac{\tilde{\theta} - \langle\tilde{\theta}\rangle}{\Theta_0} + f_c\varepsilon_{ij3}\tilde{u}_j$,

where $\tilde{\theta}$ represents the resolved potential temperature, Θ_0 is the reference temperature, $\langle \cdot \rangle_{\mathcal{H}}$ denotes a horizontal average, g is the acceleration due to gravity, f_c is the Coriolis parameter, δ_{ij} is the Kronecker delta, and ε_{ijk} is the alternating unit tensor.

The simulated ABL is horizontally homogeneous, horizontal directions are discretized pseudo-spectrally, and vertical derivatives are approximated with second-order central differences. The height of the computational domain is H , and the horizontal dimensions are L_x and L_y ; the domain is divided into N_x , N_y , and N_z uniformly spaced grid points. The grid planes are staggered in the vertical direction with the first vertical velocity plane at a distance $\tilde{\Delta}_z = \frac{H}{N_z - 1}$ from the surface, and the first horizontal velocity plane $\tilde{\Delta}_z/2$ from the surface. At the bottom, the instantaneous wall stresses are computed through the application of the Monin–Obukhov similarity theory (Porté-Agel et al. 2000; Porté-Agel 2004):

$\tau_{i3}|_w = -u_*^2 \frac{\tilde{u}_i}{U(z)} = -\left(\frac{U(z)\kappa}{\ln(z/z_0) - \Psi_M}\right)^2 \frac{\tilde{u}_i}{U(z)}$, where κ is the von Kármán constant, u_* is the friction velocity, z_0 is the roughness length, Ψ_M is the stability correction for momentum, and $U(z)$ is the plane-averaged resolved horizontal velocity. We compute the filter size using a common formulation $\tilde{\Delta} = \sqrt[3]{\tilde{\Delta}_x \tilde{\Delta}_y \tilde{\Delta}_z}$, where $\tilde{\Delta}_x = L_x/N_x$ and $\tilde{\Delta}_y = L_y/N_y$. The corresponding aliasing errors are corrected in the non-linear terms according to the 3/2 rule (e.g., Canuto et al. 1988). The time advancement is carried out using a second-order accurate Adams–Bashforth scheme (e.g., Canuto et al. 1988).

4 Neutral Atmospheric Boundary Layer

We adopt a classical numerical set-up used for previous model assessment studies (e.g., Porté-Agel et al. 2000; Porté-Agel 2004; Lu and Porté-Agel 2010). The height of the computational domain is $H = 1,000$ m, and the horizontal dimensions of the simulated volume are $L_x = L_y = 2\pi H$. We carried out simulations with resolutions of $N_x \times N_y \times N_z = 32 \times 32 \times 32$, $48 \times 48 \times 48$, $64 \times 64 \times 64$, $96 \times 96 \times 96$, and $128 \times 128 \times 128$. The simulated flow is driven by a constant pressure gradient $-u_*^2/H$ in the x -direction. We take $u_* = 0.45$ m s⁻¹ and $z_0 = 0.1$ m, which is similar to the set-up in some previous studies (e.g., Andren et al. 1994; Porté-Agel et al. 2000; Lu and Porté-Agel 2010). The upper boundary conditions are $\partial\tilde{u}/\partial z = 0$, $\partial\tilde{v}/\partial z = 0$, $\tilde{w} = 0$ and $\partial\tilde{\theta}/\partial z = 0$. At the bottom, neutral stability results in $\Psi_M = 0$. A passive scalar field, similar to that simulated in previous studies (e.g., Andren et al. 1994; Kong et al. 2000; Porté-Agel 2004; Lu and Porté-Agel 2013), is introduced into the simulations by imposing a constant downward surface flux $q_3|_w = -u_*\theta_*$.

We have collected mean and turbulent statistics after achieving statistically steady states. In the presentation, we denote the horizontal and time average as $\langle \cdot \rangle$, and the fluctuation of an arbitrary resolved variable \tilde{f} as $\tilde{f}' = \tilde{f} - \langle \tilde{f} \rangle$; on certain occasions, we take the simulations of 64^3 node and 128^3 node as base cases to present results.

4.1 First-Order Measurements

A longstanding problem in the LES of ABL flows is that the mean wind and temperature profiles differ from the similarity forms in the surface layer. In this subsection, we compare our numerical results with the predictions from similarity theory to gain a better understanding of the performance of the new closure.

The logarithmic profile, which was first published by Von Kármán in 1931, is a semi-empirical relationship used to describe the vertical distribution of horizontal wind speed above the surface within a turbulent boundary layer. The profile states that the mean streamwise

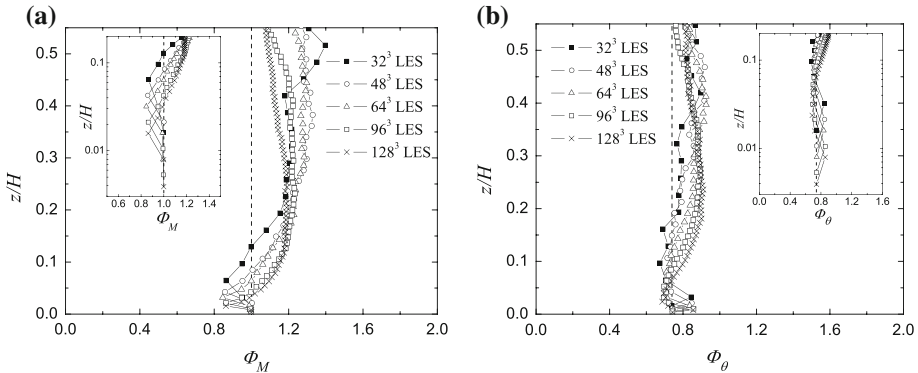


Fig. 1 Non-dimensional vertical gradient of **a** the mean resolved streamwise velocity and **b** the mean resolved scalar concentration obtained from simulations of the neutral ABL case. The *dashed line* corresponds to the classical similarity profile. The *left/right corner plots* are a zoomed view of the surface layer and they have a log scale in the *vertical direction*

velocity at a certain point in a turbulent boundary layer is proportional to the logarithm of the distance from that point to the wall. Established later, the Monin–Obukhov similarity theory, which includes thermal effects, has been experimentally confirmed in a number of field experiments (e.g., [Businger et al. 1971](#)), and represents one of the most firmly established results against which new SGS models should be compared. An example of the wind-speed profile in neutral cases can be written as the well-known logarithmic formulation: $\langle \tilde{u} \rangle = \frac{u_*}{\kappa} \ln \left(\frac{z}{z_0} \right)$. Aerodynamic roughness, z_0 , is necessarily non-zero because the log law does not apply to the viscous and roughness sublayers. The log law is a good approximation to the velocity profile in the surface layer, which occupies the lowest 10 % of the ABL. A rigorous way to evaluate model performance is to examine the values of the non-dimensional vertical gradients of the resolved streamwise velocity as a function of vertical position. The non-dimensional vertical gradient of the mean resolved streamwise velocity is defined as

$$\Phi_M = \left(\frac{\kappa z}{u_*} \right) \frac{\partial \langle \tilde{u} \rangle}{\partial z}. \tag{21}$$

On the basis of experimental results and dimensional analysis (e.g., [von Kármán 1931](#); [Businger et al. 1971](#); [Stull 1988](#)), it has been found that, in neutral cases, $\Phi_M = 1$ holds for all z in the surface layer. In this way, the logarithmic-layer mismatch can be manifested more clearly and can help quantitatively evaluate model performance. [Andren et al. \(1994\)](#) performed an extensive comparison of various LES codes using the standard Smagorinsky model with wall damping and other eddy-viscosity models. In the surface layer, their values of Φ_M were mostly > 1.2 , and some simulations yielded $\Phi_M \approx 2$. Many studies ([Mason and Thomson 1992](#); [Sullivan et al. 1994](#); [Kosović 1997](#); [Chow et al. 2005](#)) have revealed similar overshoots in Φ_M reaching over 1.5 for the standard Smagorinsky model. It appears that the standard Smagorinsky model is too dissipative, removing too much kinetic energy from the resolved field and generating a near-linear profile in the surface layer, which bears a large value of Φ_M . Figure 1a presents the non-dimensional vertical gradient of the mean resolved streamwise velocity obtained from different resolution simulations using the new closure. The new closure slightly underestimates at the third and fourth grid points (with the lowest value being about 0.85), but overall yields a value of Φ_M that remains close to 1 in the surface layer, indicative of the expected logarithmic velocity profile.

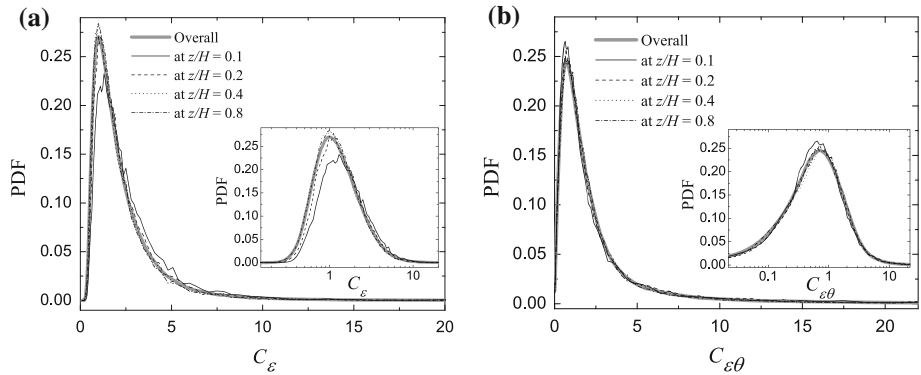


Fig. 2 Probability density functions of the dynamically calculated coefficients, **a** C_ϵ and **b** $C_{\epsilon\theta}$, obtained at different heights within the neutral ABL and overall

For the scalar counterpart, one may examine the values of the non-dimensional vertical gradients of the mean resolved scalar concentration as a function of vertical position. That non-dimensional scalar gradient is defined as

$$\Phi_\theta = \left(\frac{\kappa z}{\theta_*} \right) \frac{\partial \langle \tilde{\theta} \rangle}{\partial z}. \tag{22}$$

It has been well documented (e.g., [Businger et al. 1971](#); [Stull 1988](#)) that, in neutral cases, $\Phi_\theta = 0.74$ holds for all z in the surface layer. According to several studies (e.g., [Mason and Thomson 1992](#); [Andren et al. 1994](#); [Lu and Porté-Agel 2013](#)), standard SGS models yield values of Φ_θ that are significantly larger than 0.74 (some over 1.5). Figure 1b presents the non-dimensional vertical gradient of the mean resolved scalar concentration obtained from different resolution simulations using the new closure. The new closure slightly overestimates only at the second grid point (with the highest value being about 0.85), but overall yields a value of Φ_θ that remains close to 0.74 in the surface layer.

Further, we investigate the statistical characteristics of two model coefficients: C_ϵ and $C_{\epsilon\theta}$. Figure 2 shows the probability density functions (PDFs) of two model coefficients obtained from the 128^3 simulation. We present results obtained at four different levels as examples, and bold grey lines represent PDFs of values over all levels. The PDFs of C_ϵ and $C_{\epsilon\theta}$ show good consistency at all levels. In contrast, the PDFs of the Smagorinsky coefficient, C_s , show visible differences at different heights in the ABL ([Bou-Zeid et al. 2005](#); [Stoll and Porté-Agel 2006b, 2008](#)).

Two subplots in Fig. 2 use a logarithmic scale for the x-axis, and reveal that the fluctuations of C_ϵ and $C_{\epsilon\theta}$ follow a near log-normal distribution. For a log-normal distribution, the arithmetic mean overestimates the peak location; thus the averaged property is more readily treated by the use of the geometric mean (the geometric mean of a log-normal distribution is equal to its median) than the arithmetic mean. We adopt a procedure similar to that used in other studies ([Stoll and Porté-Agel 2006b](#)), and plot the median values of C_ϵ and $C_{\epsilon\theta}$ versus z/H in Fig. 3. Overall, the two dynamically calculated coefficients have averaged values that are approximately constant throughout the turbulent boundary layer. Recall that $C_\epsilon = 1$ and $C_{\epsilon\theta} = 1$ ([Lu and Porté-Agel 2010, 2013](#)) are reasonable values, even when based on theoretical arguments strictly validated only in the inertial subrange of high Reynolds-number turbulence.

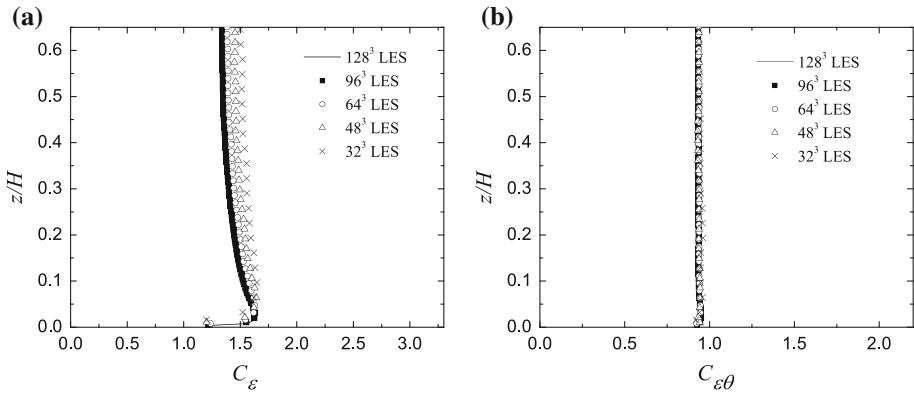


Fig. 3 Averaged values of the dynamically calculated coefficients, **a** C_ϵ and **b** $C_{\epsilon\theta}$, obtained from different resolution simulations of the neutral ABL case

4.2 Power Spectra

It is important to test the ability of LES to accurately reproduce the main spectral characteristics of the resolved field. Spectra of velocity fields in turbulent boundary layers are known to exhibit three distinct spectral scaling regions: the energy-production range, the inertial subrange and the dissipation subrange. In the case of LES of the high Reynolds-number boundary layer, the dissipation subrange is not resolved and, therefore, is not considered here. It is well known (e.g., Perry et al. 1986; Saddoughi and Veeravalli 1994; Katul and Chu 1998; Venugopal et al. 2003) that the energy spectra of the three wind components satisfy the Kolmogorov $-5/3$ power law in the inertial subrange, i.e., the range of relatively small, isotropic scales that satisfy $k_1 z \gtrsim 1$, where k_1 is the streamwise wavenumber. Also, laboratory and field measurements (e.g., Perry et al. 1986; Katul and Chu 1998; Kunkel and Marusic 2006) of boundary-layer turbulence show that, in the energy-production range corresponding to scales larger than the distance to the surface ($k_1 z \lesssim 1$) and smaller than the integral scale, spectra of the streamwise velocity component are often proportional to k_1^{-1} .

Previous LES studies have examined model performance regarding energy spectra, and limitations have been found for traditional SGS models. The spectra of the streamwise velocity obtained using the standard Smagorinsky model decay faster than the expected -1 power law in the surface layer (e.g., Andren et al. 1994; Kosović 1997; Porté-Agel et al. 2000). Within the constraints of the Smagorinsky model, this type of spectrum implies that the model dissipates kinetic energy at an excessive rate. The resulting spectra obtained using the dynamic Smagorinsky model, on the other hand, decay too slowly (the spectrum slope is close to -0.5) in the surface layer (Porté-Agel et al. 2000), likely due to the fact that the dynamic procedure samples scales near and beyond the local integral scale, at which the assumption of scale invariance of the coefficient (on which the model relies) breaks down, leading to an underestimation of the Smagorinsky coefficient near the surface (Porté-Agel et al. 2000). The lower coefficient then yields a lower energy dissipation rate and a pile-up of energy at high wavenumbers. Also, it was found that, in the inertial subrange, the dynamic Smagorinsky model may yield a streamwise velocity spectrum slope shallower (close to -0.8) than $-5/3$ (Piomelli 1993).

Figures 4 and 5 show the normalized spectra of the simulated streamwise and vertical velocity components, computed at different heights. Spectra are calculated from one-

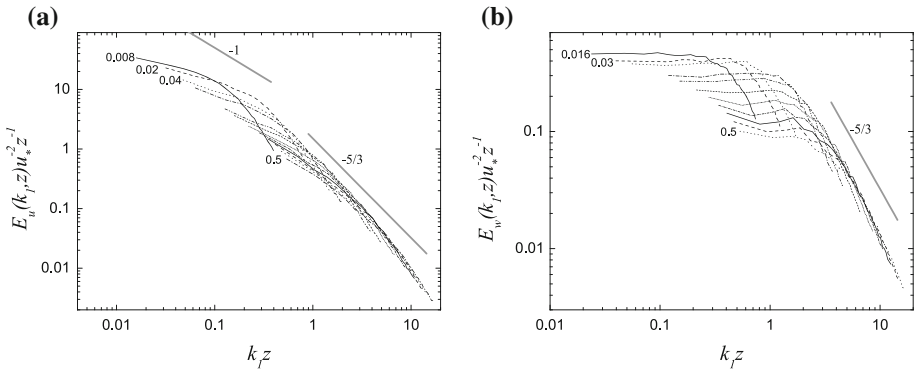


Fig. 4 Averaged non-dimensional 1-D spectra of **a** the streamwise velocity component and **b** the vertical velocity component obtained from the 64^3 simulation of the neutral ABL case. Heights (z/H) increase approximately from 0.008 to 0.5. The slopes of -1 and $-5/3$ are also shown

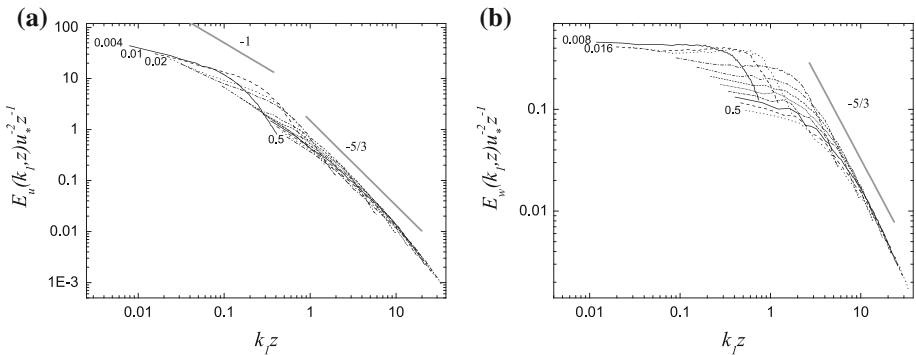


Fig. 5 Averaged non-dimensional 1-D spectra of **a** the streamwise velocity component and **b** the vertical velocity component obtained from the 128^3 simulation of the neutral ABL case. Heights (z/H) increase approximately from 0.004 to 0.5. The slopes of -1 and $-5/3$ are also shown

dimensional Fourier transforms of the velocity component and then are averaged both horizontally and in time. The streamwise wavenumber is normalized by height, and the spectrum magnitude is normalized by $u_*^2 z$. It should be noted that the spectra of the spanwise velocity component (not shown here) are similar to the spectra of the streamwise velocity component. Clearly, in the inertial subrange ($k_1 z \gtrsim 1$) all the normalized spectra show a better collapse comparing with results obtained using the standard Smagorinsky model, and are in good agreement with the $-5/3$ power law. For scales larger than the distance to the surface ($k_1 z \lesssim 1$), the slope of the spectra of the streamwise velocity component is slightly lower than -1 (close to -0.7). The spectra of the vertical velocity component differ from the spectra of the streamwise velocity component. There is no clear -1 power-law region; instead the spectra are flat in the surface layer. This finding is consistent with the expected distribution supported by theoretical (e.g., [Townsend 1976](#); [Perry et al. 1986](#)) and experimental studies (e.g., [Perry et al. 1986](#); [Katul and Chu 1998](#)). It should also be noted that, at the lowest computational levels, the spectra of both velocity components show an overly steep slope at the smallest resolved scales. At last, as expected in LES, the increase of grid resolution yields an extension of the resolved portion of the inertial subrange.

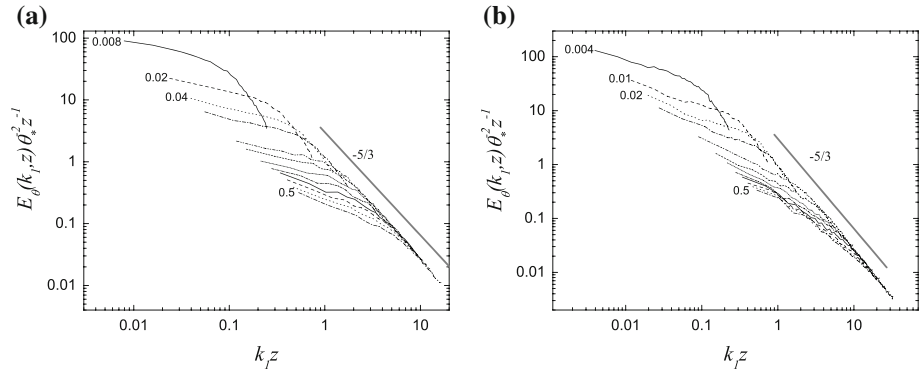


Fig. 6 Averaged non-dimensional 1-D spectra of the resolved scalar concentration obtained from **a** the 64^3 simulation of the neutral ABL case; and **b** the 128^3 simulation of the neutral ABL case. Heights (z/H) increase approximately from, **a** 0.008 to 0.5 or **b** 0.004 to 0.5. The slope $-5/3$ is also shown

The power spectrum of a scalar field is known to exhibit an inertial subrange and a dissipation subrange. In the inertial range, the spectrum follows the classical $-5/3$ power-law scaling (e.g., Sagaut 2006); as with the velocity spectrum in a neutral ABL flow, the inertial subrange should extend for the range of relatively small scales corresponding to $k_1 \gtrsim z^{-1}$. Figure 6 shows the non-dimensional 1-D power spectra obtained from the simulations using the new closure at two resolutions (64^3 and 128^3). The new approach is evidently capable of achieving the $-5/3$ power-law scaling in the inertial subrange. Also, as expected in LES, the increase of grid resolution will yield an extension of the resolved portion of the inertial subrange.

4.3 Second-Order Statistics

Averaging (both horizontally and in time) the streamwise momentum equation yields $\frac{\partial \langle \tilde{u} \tilde{w} \rangle}{\partial z} + \frac{\partial \langle \tau_{xz} \rangle}{\partial z} = -\frac{\partial \langle \bar{p} \rangle}{\partial x}$, where $\langle \tilde{u} \tilde{w} \rangle$ is the mean resolved shear stress and $\langle \tau_{xz} \rangle$ is the mean SGS shear stress. Since the simulated flow is driven by a constant pressure gradient, in the absence of viscous stresses, the normalized (by u_*^2) mean total turbulent stress grows linearly from a value of -1 at the surface to a value of zero at the top of the boundary layer. Because $\langle \tilde{w} \rangle = 0$, it is easy to prove that $\langle \tilde{u} \tilde{w} \rangle$ equals $\langle \tilde{u}' \tilde{w}' \rangle$. Mean resolved shear stress should be negative indicating an overall tendency that faster ($\tilde{u}' > 0$) fluid parcels are moving downward ($\tilde{w}' < 0$) and slower ($\tilde{u}' < 0$) fluid parcels are moving upward ($\tilde{w}' > 0$). Figure 7a shows the vertical distribution of the normalized total and partial (resolved and SGS) shear stresses obtained from the 128^3 baseline simulation and the normalized SGS stresses obtained from two coarser grids (64^3 and 96^3). As expected, the coarser resolution simulations yield SGS stresses that are larger in magnitude than the higher resolution counterparts. The distribution of total turbulent stress is indeed consistent with the expected linear behaviour. The result also serves as a confirmation of stationarity and momentum conservation of the scheme.

Figure 7b shows the vertical distributions of the normalized total and partial wall-normal fluxes obtained from the 128^3 simulation, and also includes the normalized SGS stresses and SGS fluxes obtained from two coarser grids (64^3 and 96^3). Similarly, the coarser resolution simulations yield the SGS fluxes that are larger in magnitude than the higher resolution counterparts. The similarity between the characteristics of the total turbulent stress and the total turbulent flux has been reported by direct numerical simulation (DNS) studies (e.g., Kim and

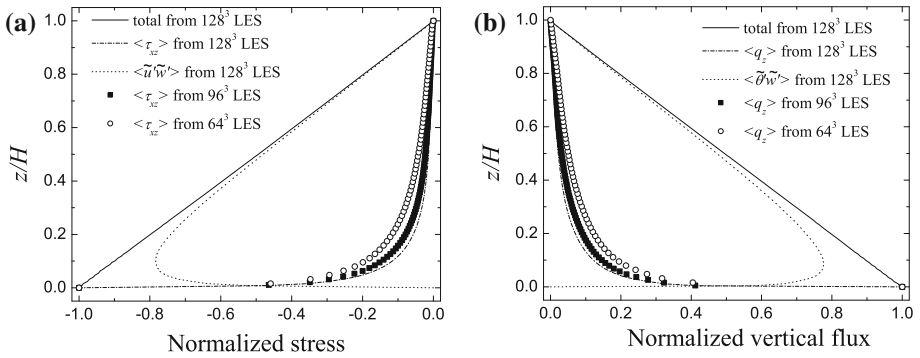


Fig. 7 Vertical distributions, in the neutral ABL, of the normalized total and partial (SGS and resolved): **a** shear stresses and **b** wall-normal fluxes

Moin 1987), indicating that productions of scalar fluctuations also take place intermittently just as that of velocity fluctuations. Also the near-linear feature of the total turbulent flux is in good agreement with both DNS results (e.g., Kim and Moin 1987; Kong et al. 2000) in the logarithmic region, and LES results (e.g., Porté-Agel 2004; Lu and Porté-Agel 2013) of a neutral ABL flow.

5 Active Scalar Modification

We now turn to the case of coupling with an active scalar (i.e. with a field that has feedback effects on the velocity field), leading to a two-way coupling between the momentum and the scalar equations. We place the emphasis on buoyancy effects. Reviews (e.g., Sagaut 2006) show that interscale energy transfers in flows are strongly affected in both stable and unstable stratification cases. This is the reason most scalar models are derived in relation to a simplified kinetic energy balance equation that includes buoyancy effects. One obtains the balance by neglecting all diffusive and convective effects, yielding an extended local equilibrium assumption

$$\varepsilon = -\tau_{ij}\tilde{S}_{ij} + \frac{g}{\Theta_0}q_3. \tag{23}$$

Recall $\varepsilon = C_\varepsilon \frac{k_{sgs}^{3/2}}{\Delta}$ and that q_3 is modelled as $\sqrt{2k_{sgs}}\theta_{sgs} \left(\frac{\tilde{G}_{\theta,3}}{|\tilde{G}_\theta|} \right)$ based on Eq. 4; thus, one obtains

$$C_\varepsilon \frac{k_{sgs}^{3/2}}{\Delta} = -2k_{sgs} \left(\frac{\tilde{G}_{ij}}{\tilde{G}_{kk}} \right) \tilde{S}_{ij} + \frac{g}{\Theta_0} \sqrt{2k_{sgs}}\theta_{sgs} \left(\frac{\tilde{G}_{\theta,3}}{|\tilde{G}_\theta|} \right). \tag{24}$$

This equation bears three solutions; we do not consider $k_{sgs} = 0$, and also we exclude another solution,¹ since it is the solution formed from $k_{sgs} = 0$ and results in an opposite trend of buoyancy effects (for instance, stably stratification should lower the SGS kinetic energy). Thus, one can arrive at the modified model expression for the SGS kinetic energy

¹ The solution is $k_{sgs} = \frac{\tilde{\Delta}^2}{C_\varepsilon^2} \left[\left(-\frac{\tilde{G}_{ij}\tilde{S}_{ij}}{\tilde{G}_{kk}} \right) - \sqrt{\left(-\frac{\tilde{G}_{ij}\tilde{S}_{ij}}{\tilde{G}_{kk}} \right)^2 + \sqrt{2} \frac{C_\varepsilon}{\Delta} \frac{g}{\Theta_0} \theta_{sgs} \left(\frac{\tilde{G}_{\theta,3}}{|\tilde{G}_\theta|} \right)} \right]^2$.

by substituting $\frac{\tilde{\Delta}}{C_{\varepsilon\theta}} \left(-\frac{\tilde{G}_{\theta,i}}{|\tilde{\mathbf{G}}_{\theta}|} \frac{\partial \tilde{\theta}}{\partial x_i} \right)$ for θ_{sgs} ,

$$k_{\text{sgs}} = \frac{\tilde{\Delta}^2}{C_{\varepsilon}^2} \left[\left(-\frac{\tilde{G}_{ij}}{\tilde{G}_{kk}} \tilde{S}_{ij} \right) + \sqrt{\left(-\frac{\tilde{G}_{ij}}{\tilde{G}_{kk}} \tilde{S}_{ij} \right)^2 + \frac{\sqrt{2}C_{\varepsilon g}}{C_{\varepsilon\theta}\Theta_0} \left(-\frac{\tilde{G}_{\theta,i}}{|\tilde{\mathbf{G}}_{\theta}|} \frac{\partial \tilde{\theta}}{\partial x_i} \right) \left(\frac{\tilde{G}_{\theta,3}}{|\tilde{\mathbf{G}}_{\theta}|} \right)} \right]^2 \tag{25}$$

It is difficult to propose a dynamic procedure because the model coefficients C_{ε} and $C_{\varepsilon\theta}$ are coupled in this expression, and so we adopt the previous simple approach, $C_{\varepsilon}/C_{\varepsilon\theta} = \sqrt{2}S_c$ (Lu and Porté-Agel 2013). Tests (e.g., Jiménez et al. 2001) have shown that the Schmidt number (or the Prandtl number depending on the physical significance of the scalar field) leads to satisfactory results. When clipping is included, the SGS kinetic energy is written as

$$k_{\text{sgs}} = \mathbf{H}(P) \frac{\tilde{\Delta}^2}{C_{\varepsilon}^2} \left[\left(-\frac{\tilde{G}_{ij}}{\tilde{G}_{kk}} \tilde{S}_{ij} \right) + \sqrt{\left(-\frac{\tilde{G}_{ij}}{\tilde{G}_{kk}} \tilde{S}_{ij} \right)^2 + H(P_{\theta}) \frac{2S_{cg}}{\Theta_0} \left(-\frac{\tilde{G}_{\theta,i}}{|\tilde{\mathbf{G}}_{\theta}|} \frac{\partial \tilde{\theta}}{\partial x_i} \right) \left(\frac{\tilde{G}_{\theta,3}}{|\tilde{\mathbf{G}}_{\theta}|} \right)} \right]^2 \tag{26}$$

The modified M_{ij} term for determining coefficients, shown in Eq. 16, is written as

$$M_{ij} = 2\alpha^2 \tilde{\Delta}^2 \left[\left(-\frac{\tilde{G}_{mn}}{\tilde{G}_{kk}} \tilde{S}_{mn} \right) + \sqrt{\left(-\frac{\tilde{G}_{mn}}{\tilde{G}_{kk}} \tilde{S}_{mn} \right)^2 + \frac{2S_{cg}}{\Theta_0} \left(-\frac{\tilde{G}_{\theta,j}}{|\tilde{\mathbf{G}}_{\theta}|} \frac{\partial \tilde{\theta}}{\partial x_j} \right) \left(\frac{\tilde{G}_{\theta,3}}{|\tilde{\mathbf{G}}_{\theta}|} \right)} \right]^2 \left(\frac{\tilde{G}_{ij}}{\tilde{G}_{ll}} \right) - 2\tilde{\Delta}^2 \left[\left(-\frac{\tilde{G}_{mn}}{\tilde{G}_{kk}} \tilde{S}_{mn} \right) + \sqrt{\left(-\frac{\tilde{G}_{mn}}{\tilde{G}_{kk}} \tilde{S}_{mn} \right)^2 + \frac{2S_{cg}}{\Theta_0} \left(-\frac{\tilde{G}_{\theta,j}}{|\tilde{\mathbf{G}}_{\theta}|} \frac{\partial \tilde{\theta}}{\partial x_j} \right) \left(\frac{\tilde{G}_{\theta,3}}{|\tilde{\mathbf{G}}_{\theta}|} \right)} \right]^2 \left(\frac{\tilde{G}_{ij}}{\tilde{G}_{ll}} \right) \tag{27}$$

We adopt $S_c = 0.71$ in this study, which is the Prandtl number of air near 20 °C.

6 Stable Atmospheric Boundary Layer

We implement the new closure in a horizontally homogeneous stable boundary layer (SBL) case. The set-up is based on a LES intercomparison study as part of the Global Energy and Water Cycle Experiment Atmospheric Boundary Layer Study (GABLES) initiative. This LES intercomparison case study, described in detail in Beare et al. (2006), represents a typical moderately stable, quasi-equilibrium ABL, similar to those commonly observed over polar regions and equilibrium nighttime conditions over land in mid latitudes. In summary, the boundary layer is driven by an imposed, uniform geostrophic wind of $U_g = 8 \text{ m s}^{-1}$; the Coriolis parameter is set to $f_c = 1.39 \times 10^{-4} \text{ rad s}^{-1}$; the initial potential temperature profile consists of a mixed layer (with potential temperature 265 K) up to 100 m with an overlying inversion of strength 0.01 K m^{-1} , and the surface (ground level) potential temperature is

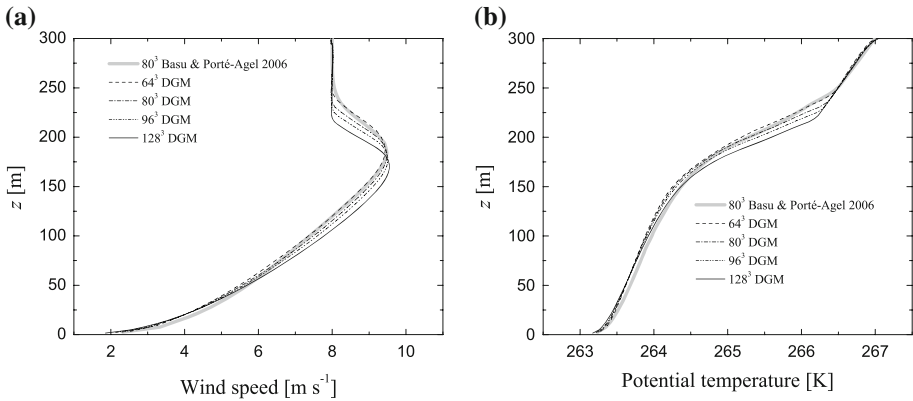


Fig. 8 Mean **a** wind speed and **b** potential temperature obtained from different resolution simulations of the GABLS case

reduced at a prescribed surface cooling rate of 0.25 K h^{-1} . The height of the computational domain is $H = 400 \text{ m}$. As suggested by [Stoll and Porté-Agel \(2008\)](#), to provide a larger range of scales (better able to capture larger buoyancy waves), the horizontal domain is twice the horizontal domain used in [Beare et al. \(2006\)](#), thus $L_x = L_y = 800 \text{ m}$. We carried out simulations with resolutions of $N_x \times N_y \times N_z = 64 \times 64 \times 64, 80 \times 80 \times 80, 96 \times 96 \times 96,$ and $128 \times 128 \times 128$. In contrast to the constant surface flux imposed in the neutral ABL case, the surface heat flux is computed through the application of surface-layer similarity theory: $q_3|_w = \frac{u_* \kappa (\theta_s - \bar{\theta})}{\ln(z/z_0) - \Psi_H}$, where θ_s is the surface (ground level) potential temperature, and Ψ_H is the stability correction for heat. Following the recommendations of the GABLS study, we adopt the roughness length $z_0 = 0.1 \text{ m}$, $\Psi_M = -4.8z/L$ and $\Psi_H = -7.8z/L$, where L is the Obukhov length. A Rayleigh damping layer above 300 m is used following the GABLS case description. More details can be found in [Beare and MacVean \(2004\)](#), [Beare et al. \(2006\)](#), [Basu and Porté-Agel \(2006\)](#), [Stoll and Porté-Agel \(2008\)](#), [Lu and Porté-Agel \(2011, 2013\)](#).

6.1 Wind Speed and Potential Temperature

Figure 8 shows the mean profiles of the resolved wind speed and potential temperature, where averaging is performed both horizontally and over the last hour of simulation. Current simulation results are also directly compared with the 80³ simulation results performed by [Basu and Porté-Agel \(2006\)](#). A low-level jet appears clearly near the top of the boundary layer, as predicted by Nieuwstadt’s theoretical model ([Nieuwstadt 1985](#)) and observed previously in simulations (e.g., [Beare et al. 2006](#); [Basu and Porté-Agel 2006](#); [Stoll and Porté-Agel 2008](#); [Lu and Porté-Agel 2013](#)). Also in agreement with other GABLS simulation results, an increase in resolution leads to a general decrease in the boundary-layer depth, an enhancement of positive curvature in the potential temperature profile in the interior of the SBL, and an increase in jet strength. Interestingly, a 64³ resolution is sufficient for the new model to yield a boundary-layer depth similar to that of the 80³ simulation performed using a local dynamic model ([Basu and Porté-Agel 2006](#)).

The Ekman spiral refers to wind or current profile near a horizontal boundary in which the flow direction rotates as one moves away from the boundary. The laminar solution produces a surface wind parallel to the surface-stress vector and at 45° to the geostrophic wind, a flow angle that is somewhat larger than that observed in real conditions. Figure 9 shows a surface

Fig. 9 Wind hodographs obtained from different resolution simulations of the GABLS case

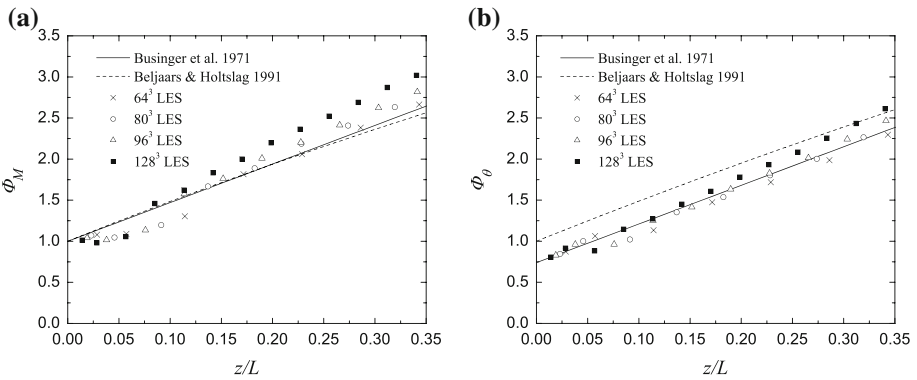
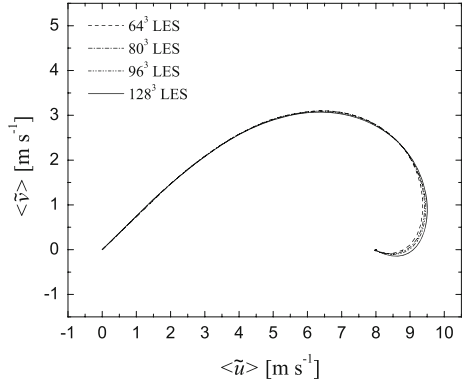


Fig. 10 Non-dimensional **a** velocity gradient and **b** temperature gradient obtained from different resolution simulations of the GABLS case. The *solid* and *dashed* lines correspond to the formulations according to Eqs. 29 and 30

flow angle of approximately 35°, which is in good agreement with most SBL cases (e.g., Kosović and Curry 2000; Basu and Porté-Agel 2006).

In SBL simulations, the non-dimensional velocity gradient, Φ_M , and the non-dimensional temperature gradient, Φ_θ , are key parameters for surface parametrizations in large-scale models and in assessments of SGS models. Owing to the existence of the non-zero mean spanwise velocity component, the definition in Eq. 21 is modified as

$$\Phi_M = \frac{\kappa z}{u_*} \sqrt{\left(\frac{\partial \langle \tilde{u} \rangle}{\partial z}\right)^2 + \left(\frac{\partial \langle \tilde{v} \rangle}{\partial z}\right)^2}, \tag{28}$$

and in the surface layer, Φ_M and Φ_θ are usually parametrized as functions of z/L . In Fig. 10, we plot the Φ_M and Φ_θ results and compare them with the formulations proposed by Businger et al. (1971)

$$\Phi_M = 1 + 4.7 \frac{z}{L}, \tag{29a}$$

$$\Phi_\theta = 0.74 + 4.7 \frac{z}{L}, \tag{29b}$$

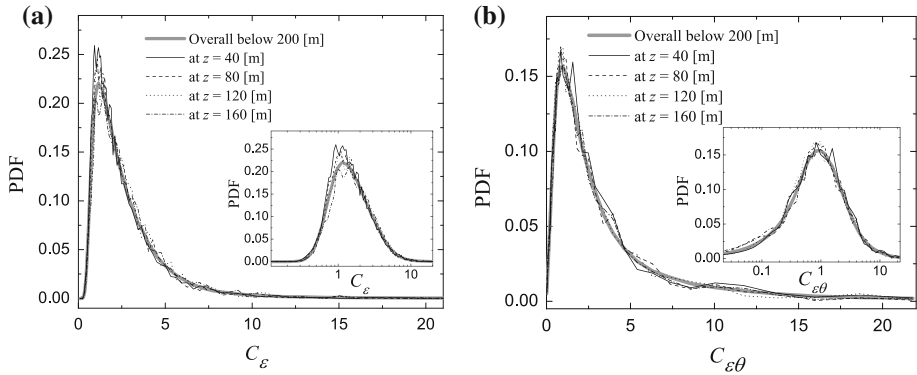


Fig. 11 Probability density functions of the dynamically calculated coefficients, **a** C_ϵ and **b** $C_{\epsilon\theta}$, obtained at different heights within the GABLS case and overall

and by [Beljaars and Holtslag \(1991\)](#)

$$\Phi_M = 1 + \frac{z}{L} \left(a + be^{-\frac{dz}{L}} \left(1 + c - \frac{dz}{L} \right) \right), \tag{30a}$$

$$\Phi_\theta = 1 + \frac{z}{L} \left(a\sqrt{1 + \frac{2az}{3L}} + be^{-\frac{dz}{L}} \left(1 + c - \frac{dz}{L} \right) \right), \tag{30b}$$

where the coefficients are $a = 1$, $b = 2/3$, $c = 5$ and $d = 0.35$. The points are from the lowest 40 m of the simulation domain. In general, all the simulation results agree quite well with the empirical relations. The non-dimensional velocity gradient is slightly underestimated for the lowest two to three grid points. With the coupling of the velocity field and the scalar field, the computed non-dimensional scalar gradient matches the similarity profiles remarkably well. In the surface layer, the results have better agreement with Eq. 29 than with Eq. 30.

Figure 11 shows the PDFs of the two model coefficients obtained from the 128³ simulation. The results are presented for four different heights and also for the whole boundary layer (bold grey lines in Fig. 11). It is clear that the PDFs of C_ϵ and $C_{\epsilon\theta}$ in the GABLS case simulations are even more consistent at all levels than those in the neutral ABL case as shown in Fig. 2.

Figure 12 shows the median values of C_ϵ and $C_{\epsilon\theta}$ versus z . Overall, the two dynamically-calculated coefficients have averaged values that are approximately constant throughout the turbulent boundary layer. Again, recall that $C_\epsilon = 1$ and $C_{\epsilon\theta} = 1$ in the GABLS case simulations ([Lu and Porté-Agel 2013](#)) are reasonable values, even when these values are based on theoretical arguments.

6.2 Turbulent Fluxes

It is important to investigate the normalized flux profiles as shown in Fig. 13. Nieuwstadt’s analytical model ([Nieuwstadt 1985](#)) predicts that the total buoyancy flux, if normalized by its surface value, should be a linear function of z/δ , where the boundary-layer depth δ is defined as $(1/0.95)$ times the height where the horizontally averaged flux falls to 5% of its surface value ([Beare et al. 2006](#)); likewise, the total normalized momentum should follow a 3/2 power law with z/δ . The intercomparison study of [Beare et al. \(2006\)](#) and the studies of [Basu and Porté-Agel \(2006\)](#), [Stoll and Porté-Agel \(2008\)](#) and [Lu and Porté-Agel \(2013\)](#) all reproduced the profiles to a high degree of accuracy. It is clear that our results follow the

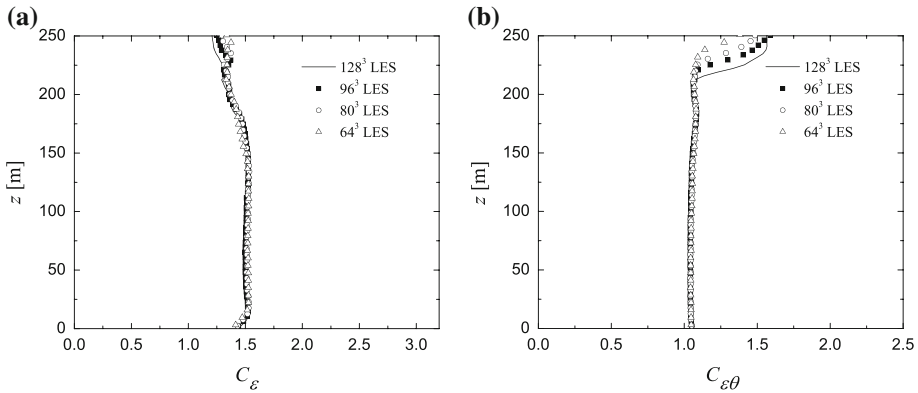


Fig. 12 Averaged values of the dynamically calculated coefficients, **a** C_ϵ and **b** $C_{\epsilon\theta}$, obtained from different resolution simulations of the GABLS case

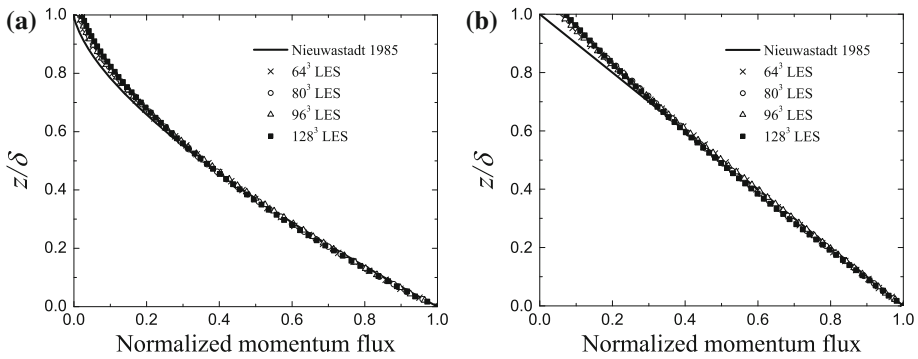


Fig. 13 Mean normalized total **a** momentum flux profiles and **b** buoyancy flux profiles obtained from different resolution simulations of the GABLS case

theoretical predictions quite closely at all resolutions, and the performance of the new model is slightly better compared with the results obtained using the non-dynamic closure of Lu and Porté-Agel (2013).

7 Lagrangian Dynamic Model

Lagrangian averaging (Meneveau et al. 1996) is a commonly used method for overcoming the intermittency of the coefficient resulting from purely local dynamic determinations. Also, Lagrangian dynamic models are well suited for the simulation of heterogeneous turbulent flows. This section presents the results of the Lagrangian version of the model in the neutral ABL case.

Following the flow backward along fluid path lines, the Lagrangian average of any quantity $A(\mathbf{x}, t)$ at time t and spatial position \mathbf{x} is defined as: $\langle A \rangle_{\mathcal{L}} = \int_{-\infty}^t A W dt'$, where $W(t - t')$ is a weighting function controlling the importance of events backwards along the path line.

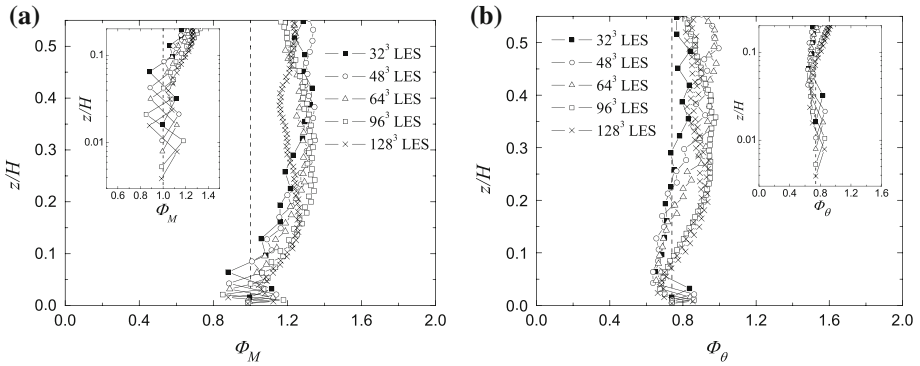


Fig. 14 Non-dimensional vertical gradient of **a** the mean resolved streamwise velocity and **b** the mean resolved scalar concentration obtained from simulations of the neutral ABL case. The *dashed line* corresponds to the classical similarity profile. The *left/right corner plot* is a zoomed view of the surface layer and it has a log scale in the *vertical direction*

The expressions for C_ε and $C_{\varepsilon\theta}$ can be written as

$$(C_\varepsilon)^{-2} = \frac{\langle L_{ij}M_{ij} \rangle_{\mathcal{L}}}{\langle M_{ij}M_{ij} \rangle_{\mathcal{L}}}, \tag{31}$$

and

$$(C_{\varepsilon\theta}C_\varepsilon)^{-2} = \frac{\langle K_iX_i \rangle_{\mathcal{L}}}{\langle X_iX_i \rangle_{\mathcal{L}}}. \tag{32}$$

For the weighting function, a common choice is the exponential formulation, $W(t - t') = (1/T)e^{-(t-t')/T}$. Based on previous studies (Meneveau et al. 1996; Bou-Zeid et al. 2005; Stoll and Porté-Agel 2006b), the time scale T is chosen as $T = 1.5\tilde{\Delta} (\langle L_{ij}M_{ij} \rangle_{\mathcal{L}} \langle M_{ij}M_{ij} \rangle_{\mathcal{L}})^{-1/8}$ for Eq. 31 and $T = 1.5\sigma_\theta \tilde{\Delta} (\langle K_iX_i \rangle_{\mathcal{L}} \langle X_iX_i \rangle_{\mathcal{L}})^{-1/4}$ for Eq. 32, where σ_θ is the standard deviation of the scalar concentration fluctuations. The Lagrangian average offers the practical advantage of allocating less weight to the recent history if the current values of $L_{ij}M_{ij}$ and K_iX_i are negative. As a result, the values of $\langle L_{ij}M_{ij} \rangle_{\mathcal{L}}$ and $\langle K_iX_i \rangle_{\mathcal{L}}$ are seldom negative. Further, when the SGS production is negative, the coefficient is not in use, and also the correlations between L_{ij} and M_{ij} and between K_i and X_i are weak. To address these issues and also to avoid sharp jumps in the coefficients, when backscatter occurs, we locally assign $L_{ij}M_{ij} = M_{ij}M_{ij}$ and $K_iX_i = X_iX_i$, which is based on the constant values used previously (Lu and Porté-Agel 2010, 2013).

The values of Φ_M and Φ_θ resulting from the Lagrangian version of the model are presented in Fig. 14. Overall, the model yields a value of Φ_M that remains close to 1, and a value of Φ_θ that remains close to 0.74, indicative of the expected similarity profiles. The non-dimensional gradients are slightly overestimated for the second lowest grid point, but the deficiencies are compensated at the third lowest grid point.

Figure 15 shows the normalized spectra obtained from the 128^3 simulation, noting that the model is evidently capable of achieving the $-5/3$ power-law scaling in the inertial subrange. The streamwise velocity spectra are slightly improved comparing with those obtained using the standard modulated gradient model (Lu and Porté-Agel 2010) and the dynamic model, which show slightly excessive dissipation near the surface.

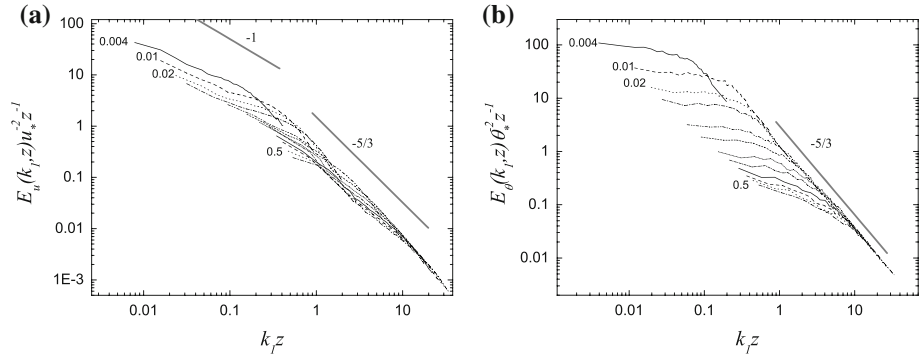


Fig. 15 Averaged non-dimensional 1-D spectra of **a** the streamwise velocity component and **b** the resolved scalar concentration obtained from the 128^3 simulation of the neutral ABL case. Heights (z/H) increase approximately from 0.004 to 0.5. The slopes of -1 and $-5/3$ are also shown

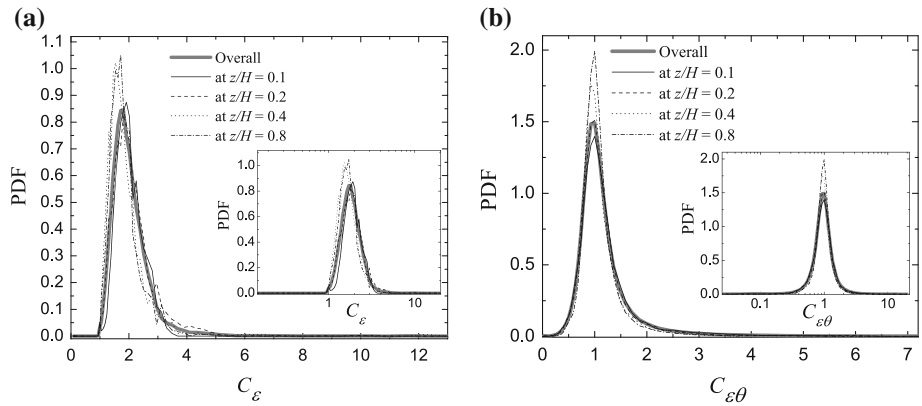


Fig. 16 Probability density functions of the dynamically calculated coefficients, **a** C_ϵ and **b** $C_{\epsilon\theta}$, obtained at different heights within the neutral ABL and overall

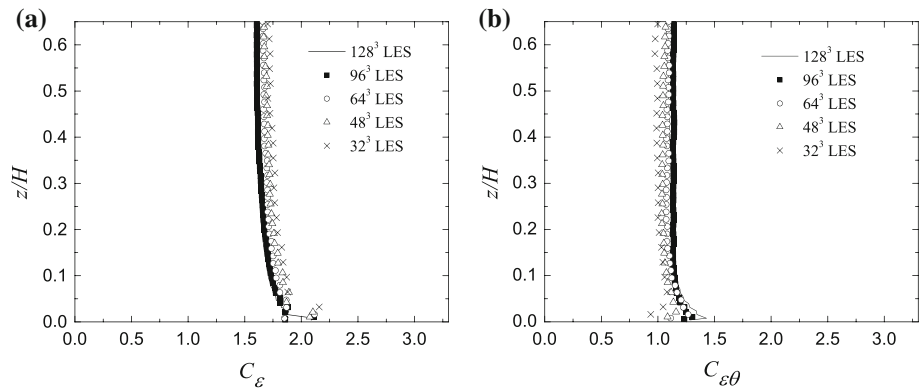


Fig. 17 Averaged values of the dynamically calculated coefficients **a** C_ϵ and **b** $C_{\epsilon\theta}$, obtained from different resolution simulations of the neutral ABL case

The PDFs of the coefficients, shown in Fig. 16, are very similar at all levels and reveal that the fluctuations follow a near log-normal distribution. Figure 17 shows that, overall, the dynamically calculated coefficients have averaged values that are approximately constant throughout the turbulent boundary layer.

8 Summary

We have developed a dynamic non-linear SGS closure for LES. The complete SGS model bears most of the desirable characteristics of a non-viscosity gradient SGS stress model (Lu and Porté-Agel 2010; Lu 2011) and a non-diffusivity SGS flux model (Lu and Porté-Agel 2013). In contrast to the original model, the proposed closure is tuning-free because it uses the Germano identity (Germano et al. 1991; Lilly 1992) between the resolved (Leonard) stresses/fluxes and the SGS stresses/fluxes to dynamically compute the two model coefficients.

It is well known that in the surface layer of the ABL, where SGS motions contribute to a large fraction of the total turbulent fluxes, LES is rather sensitive to SGS parametrization. Traditional closures yield deviations from the Monin–Obukhov similarity forms in the surface layer. The deviations are readily observed in the wind-speed and temperature profiles, and to a greater extent in their dimensionless vertical derivatives. The potential of the new closure is presented in simulations of a well-established neutrally stratified ABL case and a well-known stably stratified ABL case. Overall, numerical results are in good agreement with reference results (based on observations, well-established empirical formulations and theoretical predictions of a variety of flow statistics).

This study also reveals that the PDFs of C_ε and $C_{\varepsilon\theta}$ are near log-normal, and median values of the two model coefficients are approximately constant (close to the theoretical values) throughout the turbulent boundary layer. The latter explains the reason why, in previous ABL simulations and simulations of other types of fluid flow (Lu and Porté-Agel 2010, 2013; Lu 2011; Cheng and Porté-Agel 2013), satisfactory results were achieved using constant coefficients. This gives the closure an advantage over the standard Smagorinsky model, which bears the issue that the optimum value of the constant model coefficient, C_s , varies greatly depending on the local flow conditions.

Despite the good performance exhibited by the new closure, it is based on the assumption of local equilibrium. Possible future modifications of the model include the development and testing of alternative ways of computing the magnitude of the SGS flux (e.g., solving additional equations for both the SGS kinetic energy and the SGS scalar variance).

Acknowledgments This research was supported by the Swiss National Science Foundation (Grants 200021_132122 and IZERZ0_142236), and the US National Science Foundation (Grant ATM-0854766). Computing resources were provided by the Minnesota Supercomputing Institute and the Swiss National Supercomputing Centre. The authors wish to thank the editor and the anonymous reviewer for their helpful comments.

References

- Albertson JD, Parlange MB (1999) Natural integration of scalar fluxes from complex terrain. *Adv Water Resour* 23:239–252
- Andren A, Brown AR, Graf J, Mason PJ, Moeng CH, Nieuwstadt FTM, Schumann U (1994) Large-eddy simulation of a neutrally stratified boundary layer: a comparison of four computer codes. *Q J R Meteorol Soc* 120(520):1457–1484

- Basu S, Porté-Agel F (2006) Large-eddy simulation of stably stratified atmospheric boundary layer turbulence: a scale-dependent dynamic modelling approach. *J Atmos Sci* 63:2074–2091
- Beare RJ, MacVean MK (2004) Resolution sensitivity and scaling of large-eddy simulations of the stable boundary layer. *Boundary-Layer Meteorol* 112(2):257–281
- Beare RJ, MacVean MK, Holtslag AAM, Cuxart J, Esau I, Golaz JC, Jimenez MA, Khairoutdinov M, Kosovic B, Lewellen D, Lund TS, Lundquist JK, McCabe A, Moene AF, Noh Y, Raasch S, Sullivan P (2006) An intercomparison of large-eddy simulations of the stable boundary layer. *Boundary-Layer Meteorol* 118(2):247–272
- Beljaars ACM, Holtslag AAM (1991) Flux parameterization over land surfaces for atmospheric models. *J Appl Meteorol* 30:327–341
- Bou-Zeid E, Meneveau C, Parlange M (2005) A scale-dependent Lagrangian dynamic model for large eddy simulation of complex turbulent flows. *Phys Fluids* 17:025105
- Businger JA, Wynagaard JC, Izumi Y, Bradley EF (1971) Flux–profile relationships in the atmospheric surface layer. *J Atmos Sci* 28:181–189
- Cambon C, Mansour NN, Godeferd FS (1997) Energy transfer in rotating turbulence. *J Fluid Mech* 337:303–332
- Canuto C, Hussaini MY, Quarteroni A, Zang TA (1988) *Spectral methods in fluid dynamics*. Springer, Berlin, 567 pp
- Chamecki M (2010) Modeling subgrid-scale heat fluxes in the neutral and stratified atmospheric boundary layer. *J Turbul* 11(13):1–16
- Cheng WC, Porté-Agel F (2013) Evaluation of subgrid-scale models in large-eddy simulation of flow past a two-dimensional block. *Int J Heat Fluid Flow* 44:301–311
- Chow FK, Street RL, Xue M, Ferziger JH (2005) Explicit filtering and reconstruction turbulence modelling for large-eddy simulation of neutral boundary layer flow. *J Atmos Sci* 62:2058–2077
- Chumakov SG, Rutland CJ (2005) Dynamic structure subgrid-scale models for large eddy simulation. *Int J Numer Methods Fluids* 47:911–923
- Clark RA, Ferziger JH, Reynolds WC (1979) Evaluation of subgrid-scale models using an accurately simulated turbulent flow. *J Fluid Mech* 91(1):1–16
- Deardorff JW (1970) A numerical study of three-dimensional turbulent channel flow at large Reynolds numbers. *J Fluid Mech* 41:453–480
- Deardorff JW (1972) Numerical investigation of neutral and unstable planetary boundary layers. *J Atmos Sci* 29:91–115
- Germano M, Piomelli U, Cabot WH (1991) A dynamic subgrid-scale eddy viscosity model. *Phys Fluids A* 3(7):1760–1765
- Higgins CW, Parlange MB, Meneveau C (2003) Alignment trends of velocity gradients and subgrid-scale fluxes in the turbulent atmospheric boundary layer. *Boundary-Layer Meteorol* 109(1):59–83
- Holtslag B (2006) Preface: GEWEX atmospheric boundary-layer study GABLS on stable boundary layers. *Boundary-Layer Meteorol* 118(2):243–246
- Horiuti K (2006) Transformation properties of dynamic subgrid-scale models in a frame of reference undergoing rotation. *J Turbul* 7(16):1–27
- Jiménez C, Ducros F, Cuenot B, Bédard B (2001) Subgrid scale variance and dissipation of a scalar field in large eddy simulations. *Phys Fluids* 13(6):1748–1754
- Juneja A, Brasseur JG (1999) Characteristics of subgrid-resolved-scale dynamics in anisotropic turbulence, with application to rough-wall boundary layers. *Phys Fluids* 11(10):3054–3068
- Katul GG, Chu CR (1998) A theoretical and experimental investigation of energy-containing scales in the dynamic sublayer of boundary-layer flows. *Boundary-Layer Meteorol* 86(2):279–312
- Khanna S, Brasseur JG (1998) Three-dimensional buoyancy- and shear-induced local structure of the atmospheric boundary layer. *J Atmos Sci* 55:710–743
- Kim J, Moin P (1987) Transport of passive scalars in a turbulent channel flow. In: *Proceedings of the 6th international symposium on turbulent shear flows*, Toulouse, France, 7–9 September 1987. Springer, Berlin
- Kobayashi H, Shimomura Y (2001) The performance of dynamic subgrid-scale models in the large eddy simulation of rotating homogeneous turbulence. *Phys Fluids* 13(8):2350–2360
- Kong H, Choi H, Lee JS (2000) Direct numerical simulation of turbulent thermal boundary layers. *Phys Fluids* 12(10):2555–2568
- Kosović B (1997) Subgrid-scale modelling for the large-eddy simulation of high-Reynolds-number boundary layers. *J Fluid Mech* 336:151–182
- Kosović B, Curry JA (2000) A large eddy simulation study of a quasi-steady, stably stratified atmospheric boundary layer. *J Atmos Sci* 57:1052–1068
- Kunkel GJ, Marusic I (2006) Study of the near-wall-turbulent region of the high-Reynolds-number boundary layer using an atmospheric flow. *J Fluid Mech* 548:375–402

- Lilly DK (1992) A proposed modification of the Germano subgrid-scale closure method. *Phys Fluids* 4(3):633–635
- Liu S, Meneveau C, Katz J (1994) On the properties of similarity subgrid-scale models as deduced from measurements in a turbulent jet. *J Fluid Mech* 275:83–119
- Lu H (2011) Assessment of the modulated gradient model in decaying isotropic turbulence. *Theor Appl Mech Lett* 1:041004
- Lu H, Porté-Agel F (2010) A modulated gradient model for large-eddy simulation: application to a neutral atmospheric boundary layer. *Phys Fluids* 22:015109
- Lu H, Porté-Agel F (2011) Large-eddy simulation of a very large wind farm in a stable atmospheric boundary layer. *Phys Fluids* 23:065101
- Lu H, Porté-Agel F (2013) A modulated gradient model for scalar transport in large-eddy simulation of the atmospheric boundary layer. *Phys Fluids* 25:015110
- Lu H, Rutland CJ, Smith LM (2007) A priori tests of one-equation LES modelling of rotating turbulence. *J Turbul* 8(37):1–27
- Lu H, Rutland CJ, Smith LM (2008) A posteriori tests of one-equation LES modelling of rotating turbulence. *Int J Mod Phys C* 19:1949–1964
- Mason PJ (1989) Large-eddy simulation of the convective atmospheric boundary layer. *J Atmos Sci* 46(11):1492–1516
- Mason PJ, Thomson DJ (1992) Stochastic backscatter in large-eddy simulations of boundary layers. *J Fluid Mech* 242:51–78
- Meneveau C, Lund TS, Cabot WH (1996) A Lagrangian dynamic subgrid-scale model of turbulence. *J Fluid Mech* 319:353–385
- Menon S, Yeung PK, Kim WW (1996) Effect of subgrid models on the computed interscale energy transfer in isotropic turbulence. *Comput Fluids* 25(2):165–180
- Nieuwstadt FTM (1985) A model for the stationary, stable boundary layer. In: Hunt JCR (ed) *Turbulence and diffusion in stable environments*. Oxford University Press, Oxford, pp 149–179
- Perry AE, Henbest S, Chong MS (1986) A theoretical and experimental study of wall turbulence. *J Fluid Mech* 165:163–199
- Piomelli U (1993) High Reynolds number calculations using the dynamic subgrid-scale stress model. *Phys Fluids* 5:1484–1490
- Porté-Agel F (2004) A scale-dependent dynamic model for scalar transport in large-eddy simulations of the atmospheric boundary layer. *Boundary-Layer Meteorol* 112(1):81–105
- Porté-Agel F, Meneveau C, Parlange MB (2000) A scale-dependent dynamic model for large-eddy simulation: application to a neutral atmospheric boundary layer. *J Fluid Mech* 415:261–284
- Porté-Agel F, Meneveau C, Parlange MB, Eichinger WE (2001) A priori field study of the subgrid-scale heat fluxes and dissipation in the atmospheric surface layer. *J Atmos Sci* 58:2673–2698
- Saddoughi SG, Veeravalli SV (1994) Local isotropy in turbulent boundary layers at high Reynolds number. *J Fluid Mech* 268:333–372
- Sagaut P (2006) *Large eddy simulation for incompressible flows*, 3rd edn. Springer, Berlin, 556 pp
- Smagorinsky J (1963) General circulation experiments with the primitive equations: I the basic experiment. *Mon Weather Rev* 91(3):99–164
- Smith LM, Waleffe F (1999) Transfer of energy to two-dimensional large scales in forced, rotating three-dimensional turbulence. *Phys Fluids* 11(6):1608–1622
- Stoll R, Porté-Agel F (2006a) Effect of roughness on surface boundary conditions for large-eddy simulation. *Boundary-Layer Meteorol* 118(1):169–187
- Stoll R, Porté-Agel F (2006b) Dynamic subgrid-scale models for momentum and scalar fluxes in large-eddy simulations of neutrally stratified atmospheric boundary layers over heterogeneous terrain. *Water Resour Res* 42:W01409
- Stoll R, Porté-Agel F (2008) Large-eddy simulation of the stable atmospheric boundary layer using dynamic models with different averaging schemes. *Boundary-Layer Meteorol* 126(1):1–28
- Stull RB (1988) *An introduction to boundary-layer meteorology*. Kluwer, Dordrecht, 666 pp
- Sullivan PE, McWilliams JC, Moeng CH (1994) A subgrid-scale model for large-eddy simulation of planetary boundary-layer flows. *Boundary-Layer Meteorol* 71(3):247–276
- Townsend AA (1976) *The structure of turbulent shear flow*, 2nd edn. Cambridge University Press, Cambridge, 429 pp
- Venugopal V, Porté-Agel F, Fofoula-Georgiou E, Carper M (2003) Multiscale interactions between surface shear stress and velocity in turbulent boundary layers. *J Geophys Res* 108:4613
- von Kármán T (1931) *Mechanical similitude and turbulence*. Technical memorandum no 611, NACA, Washington, DC